

# Indentation size effects of ferritic/martensitic steels: A comparative experimental and modelling study

Ana Ruiz-Moreno\*, Peter Hähner

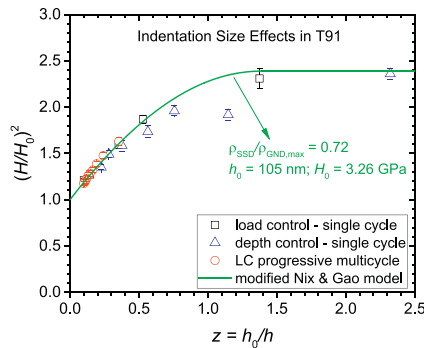
European Commission, DG Joint Research Centre, Nuclear Safety and Security Directorate, Westerduinweg 3, 1755 LE Petten, The Netherlands



## HIGHLIGHTS

- Quasi-static nanoindentation properties are measurement mode independent.
- The parameters of dynamic oscillations influence the indentation size effect (ISE).
- A new modified Nix–Gao model accounts for the break-down of the ISE scaling regime.
- The new ISE model predicts the high dislocation densities of martensitic laths.

## GRAPHICAL ABSTRACT



## ARTICLE INFO

### Article history:

Received 23 January 2018

Received in revised form 22 February 2018

Accepted 23 February 2018

Available online 24 February 2018

### Keywords:

Nanoindentation

Continuous stiffness measurements

Ferritic/martensitic steels

Indentation size effect

Dislocation density

Nix–Gao model

## ABSTRACT

The paper presents a comparative study of different nanoindentation methods as applied to the ferritic/martensitic steels T91 and Eurofer97, here investigated in the non-irradiated reference state, but envisaged as structural materials for nuclear fission and fusion applications, respectively. Depth-controlled single cycle measurements at various indentation depths, force-controlled single cycle, force-controlled progressive multi-cycle measurements, and continuous stiffness measurements (CSM) using a Berkovich tip at room temperature have been combined to determine the indentation hardness and the elastic modulus, and to assess the robustness of the different methods in capturing the indentation size effects (ISE) of those steels. The Nix–Gao model is found inappropriate because it does not account for the breakdown of the scaling regime at small indentation depths that is linked to the extremely high density of dislocations associated with martensitic lath boundary misorientation. A generalization of the Nix–Gao model is therefore developed which allows the prediction of the dislocation densities in the lath structure in accordance with neutron diffraction results. Amplitude and frequency of the CSM oscillations influence the ISE observed. Differences of the microstructure-based parameters describing the ISE of quasi-static and dynamic measurements on T91 and Eurofer97 may reflect differences in the associated deformation mechanisms and histories.

© 2018 The Authors. Published by Elsevier Ltd. This is an open access article under the CC BY-NC-ND license (<http://creativecommons.org/licenses/by-nc-nd/4.0/>).

## 1. Introduction

High strength ferritic/martensitic (F/M) steels are candidate materials for structural components in next generation nuclear fission and fusion reactors owing to their superior corrosion and irradiation resistance, as well as their good mechanical performance in terms of creep

\* Corresponding author.

E-mail address: [ana.ruiz-moreno@ec.europa.eu](mailto:ana.ruiz-moreno@ec.europa.eu) (A. Ruiz-Moreno).

**Table 1**  
Chemical composition of the T91 and Eurofer97 materials (in wt%; Fe balance).

	Cr	Mo	Mn	Si	V	Ni	Nb	Cu
<b>T91</b>	8.873	0.871	0.386	0.218	0.195	0.115	0.077	0.080
<b>Eurofer97</b>	8.87	<0.001	0.42	0.06	0.19	0.0075	<0.001	0.021
	Al	C	N	P	S	Sn	O	
<b>T91</b>	0.009	0.097	0.0440	0.020	0.0005	-	-	
<b>Eurofer97</b>	0.008	0.12	0.018	0.004	0.003	<0.005	0.001	
	W	Ta	Ti	Co	As	Sb	Zr	
<b>T91</b>	-	-	-	-	-	-	-	
<b>Eurofer97</b>	1.10	0.14	0.008	0.005	<0.005	<0.005	<0.005	

and fatigue life. Understanding their deformation behaviour under high irradiation dose and high temperature is important to predict the component lifetimes at operating conditions. Recent advances in small specimen and micromechanical testing have promoted the assessment of radiation damage, either ion- or neutron-induced, thanks to the capability of testing shallow depths and minimized volumes of activated materials [1–3]. Furthermore, small scale mechanical testing is used for validating mechanism-based computational material engineering, since the relevant length scales can be addressed by modelling and

experiments, leading to improved understanding and extrapolation of the long-term performance of materials [4]. Amongst the micromechanical testing techniques explored by the scientific community, nanoindentation is the most widely developed and used so far. Continuous improvements in methodologies to record and analyse load-displacement curves are promoting nanoindentation to complement conventional mechanical testing in materials selection and design [5]. In addition, small indentations are virtually non-destructive for larger components, while, through sectioning, the technique allows the testing of positions with varying properties across the thickness, such as graded ion-irradiated layers or welded joints, the assessment of which is of interest to nuclear safety and beyond.

Nowadays, nanoindentation devices offer the possibility to continuously probe the stiffness of a material at increasing depths, and thereby derive hardness and elastic modulus, by superimposing a small oscillating force on the quasi-static load cycle applied in traditional nanoindentation. However, an oscillation softening effect generally occurs in metals [6], and the derived mechanical properties depend on the magnitude and frequency of the oscillation [7,8]. Therefore, further studies are needed to understand if and to what extent dynamic measurements in continuous stiffness measurement (CSM) mode, influence the outcome of the tests.

While the measured indentation hardness depends on the material properties, like elasticity, yield stress and strain hardening behaviour,

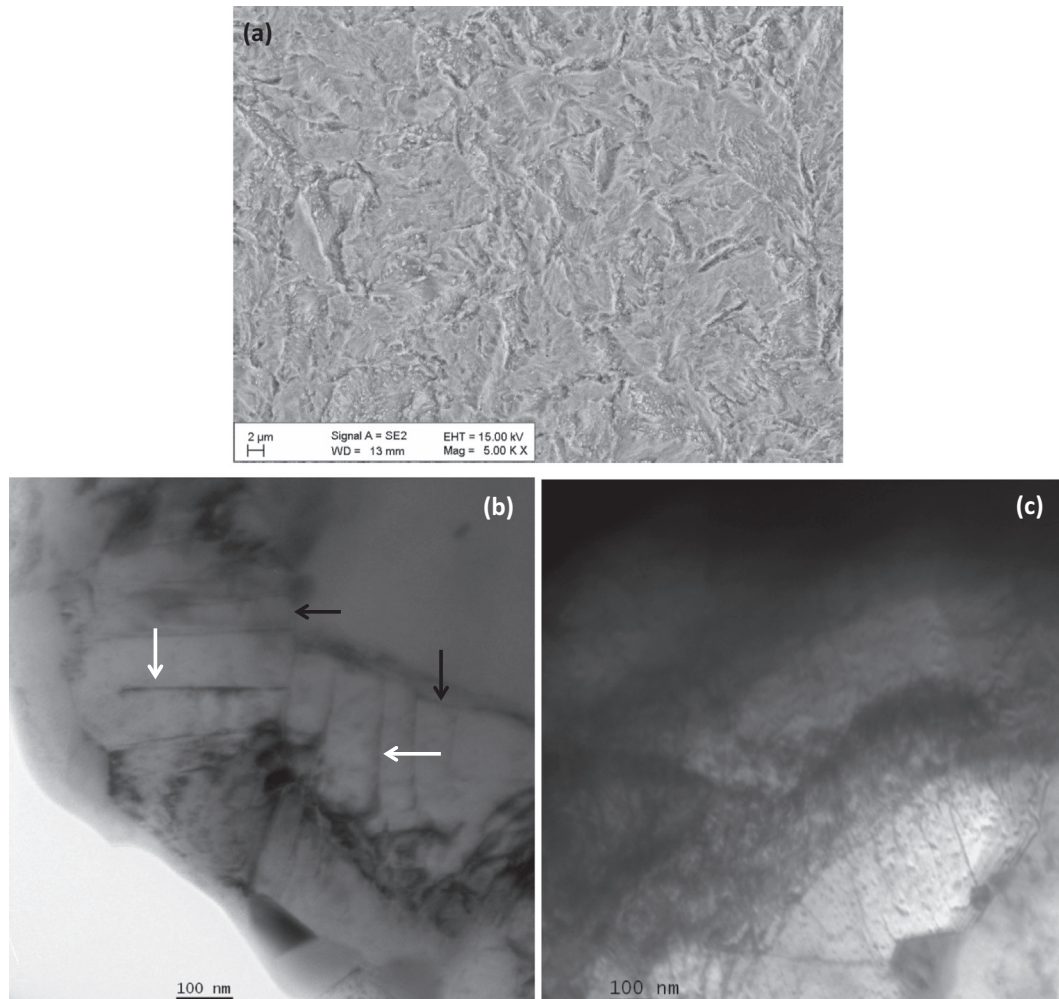


**Fig. 1.** Microstructure of T91 imaged by SEM (a) and TEM (b, c) evidencing dislocation arrays (white arrows in b) transverse to lath boundaries (black arrows) and tangles of high dislocation density inside martensite laths (c).

it is well known that it is also affected by instrumentation and testing parameters, such as the indenter geometry and the indentation size [8–10]. Since Nix and Gao in 1998 [11] first established a universal scaling relation between the indentation hardness and depth, several refinements of the theory have appeared accounting for the material microstructure [12,13]. Such indentation size effects (ISE), which represent a manifestation of the ‘smaller is stronger’ paradigm, offer a powerful means for the quantitative assessment of microstructural features and, in particular, changes thereof relating to materials ageing and damage [14,15].

In this framework, the present work reports results from an extensive nanoindentation characterization of the F/M steels T91 and Eurofer97 by quasi-static and dynamic measurements, in order to extract hardness and elastic modulus as functions of indentation depth, and to perform a comparative study of the ISE as captured by the different methods. F/M steels with associated lath structure are known to exhibit very high dislocation densities associated with lath boundary misorientation; dislocation densities can exceed  $10^{15} \text{ m}^{-2}$ , as observed by time-of-flight neutron diffraction in as-quenched martensite steel [16]. In this work we investigate how these dislocation densities can be quantitatively determined by observing the ISE, which leads us to proposing a modification of the Nix–Gao model, in order to cope with those high dislocation densities and the concomitant breakdown of the scaling behaviour. This is achieved by modifying the density profile of the geometrically necessary dislocations. The predictions of the generalized model are discussed and applied to an evaluation of the ISE of the F/M steels.

## 2. Experimental

### 2.1. Materials and methods

Two F/M steels, namely T91 and Eurofer97, have been used for this study. The materials were cut into plates of 1 mm thickness and manually polished with successively finer grinders and polishing solutions. Grinding started first using a 320 grit paper to remove about 50  $\mu\text{m}$  thickness, and was then continued using a 1200 grit paper. Polishing was done using MD Allegro water-based diamond suspensions of 9  $\mu\text{m}$ , 3  $\mu\text{m}$  and 1  $\mu\text{m}$  grain sizes. A final oxide polishing step was gently done for 5 min using colloidal silica particles. The roughness of the surface was checked by Atomic Force Microscopy to be below 20 nm. The chemical composition of both steels is given in Table 1. T91 specimens were cut from a hot rolled plate normalized at 1050 °C during 1 min/mm (per mm thickness), quenched to room temperature, tempered at 770 °C for 3 min/mm and then cooled in air. Eurofer97 samples were cut from broken Charpy specimens prepared from forged bars hardened at 979 °C for 1 h 51 min and tempered at 739 °C for 3 h 42 min.

The microstructure of the two F/M materials was imaged by scanning electron microscopy (SEM) (Zeiss, Leo Supra 50) and transmission electron microscopy (TEM) (FEI, Tecnai 20) at an accelerating voltage of 15 kV and 200 kV, respectively. For the SEM analysis, one sample of each material was etched in Michel's solution. The striated structure of martensite laths can be seen in the SEM micrographs of Fig. 1, while the high magnification TEM images show dislocation arrays formed in a quasi-perpendicular direction to lath boundaries (Fig. 1b) and tangles of high dislocation density which are characteristic of martensite lath structure (Fig. 1c).

Indentation tests were conducted using a high temperature Ultra Nanoindentation test device UNHT<sup>3</sup> HTV from Anton Paar, featuring dual indenters (indentation and active reference tip) that provide active surface referencing and minimise drift and frame compliance. A Berkovich diamond tip was used for the indentation tests. The tip area function and the frame compliance were calibrated according to ISO 14577-2 using the Datasure IIT kit of certified reference materials (tungsten, W, and fused silica, FS) from NPL and following an iterative approach [17]. For the calibration, standard indentations (30 s loading ramp, 10 s hold time at maximum load, 30 s unloading ramp) were

performed on W from 10 mN to 100 mN maximum force, while on FS the force range extended from 0.2 mN to 100 mN. The frame compliance was calculated by the measurements on W as the intercept of the plot of total compliance,  $C_t$ , versus the inverse of the square root of the contact area,  $1/\sqrt{A_c}$ . The tip area function was determined by adjusting a spline interpolation to the FS measurements of the projected area,  $A_p$ , versus contact depth,  $h_c$ ; where  $A_p$  was calculated from the stiffness measurements using  $A_p = \frac{\pi}{4\beta^2} \frac{S^2}{E_c^2}$ . For the first iteration, the area function of a perfect Berkovich tip was used ( $A_0 = 24.5 h_c^2$ ). Convergence was achieved after two iterations resulting in the frame compliance determined to amount to 0.325 nm/mN.

Four different nanoindentation measurement modes have been applied for the comparison of ISE. Force controlled single cycles (FSC) up to maximum forces,  $F_{\text{max}}$ , ranging from 1 mN to 100 mN, as well as depth controlled single cycles (DSC) up to maximum depths,  $h_{\text{max}}$ , ranging from 50 nm to 500 nm, were performed using 30 s of loading and unloading ramp times and 10 s dwelling at maximum force. Progressive multi-cycles in force control (PMC) were performed applying 10 consecutive loading-unloading cycles with the load being increased by  $0.1F_{\text{max}}$  in each cycle from 10 mN to 100 mN.

The dynamic measurements were performed in force controlled CSM mode, where a sinusoidal oscillation is superimposed to a base load increasing linearly up to 100 mN with again 30 s loading and unloading times and 10 s dwell time. Different amplitudes and frequencies of the superimposed sinus were tested; with amplitudes ranging from 5% to 20% of  $F_{\text{max}}$ , and frequencies from 10 Hz to 100 Hz. Fig. 2(a)

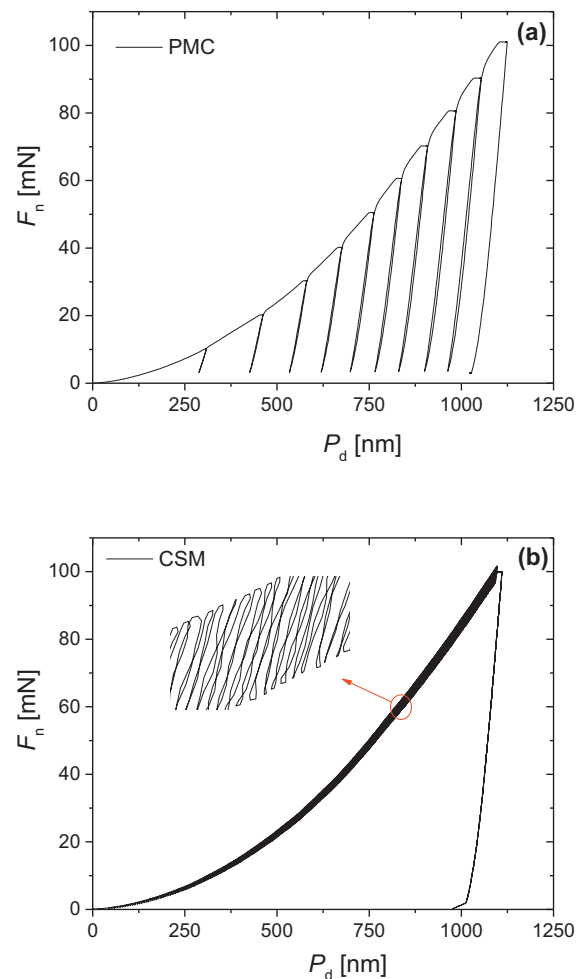


Fig. 2. Examples of nanoindentation load–displacement curves of T91 measured by PMC (a) and CSM (b).

and (b) illustrate examples of load–displacement curves recorded applying the PMC and CSM method, respectively.

The spacing between indentations was always 50  $\mu\text{m}$ , even for the shallower indents. The zero contact point was automatically determined by setting a contact stiffness threshold, either 300  $\mu\text{N}/\mu\text{m}$  or 500  $\mu\text{N}/\mu\text{m}$ , above which the indenter is considered to be in touch with the surface. After completing the measurements, the automatic contact point detection was checked and manually corrected whenever necessary.

## 2.2. Quasi-static measurements

Quasi-static measurements were repeated 15 times at different surface positions for each  $F_{\text{max}}$  and  $h_{\text{max}}$  of the FSC and DSC test methods, while for each PMC measurement (15 repeats) all 10 force levels were applied at the same surface position. The data were analysed according to ISO-14577-1 by fitting the 98% to 40% portion of the unloading curve to the power law of Eq. (1), and using the fitted parameters to calculate the contact depth  $h_c$ , and the stiffness  $S$ , by Eqs. (2) and (3)

$$F = F_{\text{max}} \left( \frac{h - h_p}{h_{\text{max}} - h_p} \right)^m \quad (1)$$

$$h_c = h_{\text{max}} - \varepsilon(h_{\text{max}} - h_r) \quad (2)$$

$$S = \frac{m F_{\text{max}}}{h_{\text{max}} - h_p} \quad (3)$$

where  $h_p$  is the permanent depth after force removal,  $h_{\text{max}}$  is the depth at maximum load,  $h_r$  is the tangent depth and  $\varepsilon \approx 0.75$  is a variable which weakly depends on the fitted exponent  $m$  [18]. Indentation hardness  $H_{\text{IT}}$ , and reduced plane strain modulus of the contact  $E_r$ , are then determined by the projected area of contact between the indenter and the sample,  $A_p$ , according to Eqs. (4) and (5):

$$H_{\text{IT}} = \frac{F_{\text{max}}}{A_p(h_c)} \quad (4)$$

$$E_r = \frac{\sqrt{\pi} S}{2\beta \sqrt{A_p(h_c)}} \quad (5)$$

where  $\beta$  is a geometric factor set to 1.034 for a Berkovich indenter. The indentation modulus was then obtained from the reduced modulus according to

$$E_{\text{IT}} = \frac{1 - \nu_s^2}{\frac{1}{E_r} - \frac{1 - \nu_i^2}{E_i}} \quad (6)$$

using as Poisson ratio of the steel samples,  $\nu_s = 0.3$ , and as Poisson ratio of the diamond indenter,  $\nu_i = 0.07$  and the indenter modulus  $E_i = 1141 \text{ GPa}$ .

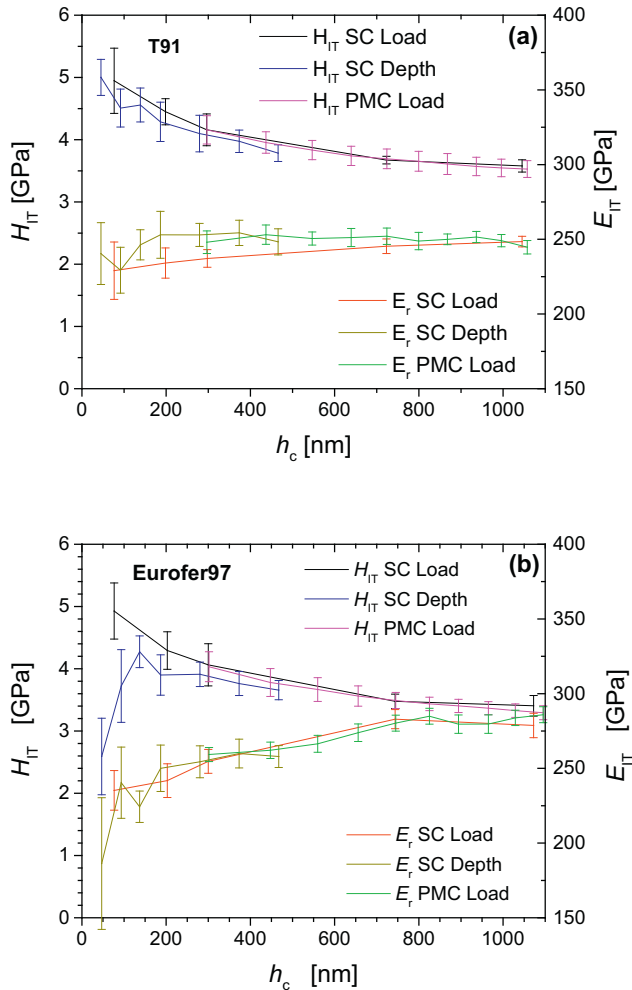


**Fig. 3.** Indentation hardness  $H_{\text{IT}}$ , and indentation elastic modulus  $E_{\text{IT}}$ , of T91 (a) and Eurofer97 (b) measured quasi-statically by single cycles in load control, in depth control, and progressive multi-cycling in load control. Each data point represents the average of 15 repeats with standard deviation as indicated by the error bars.

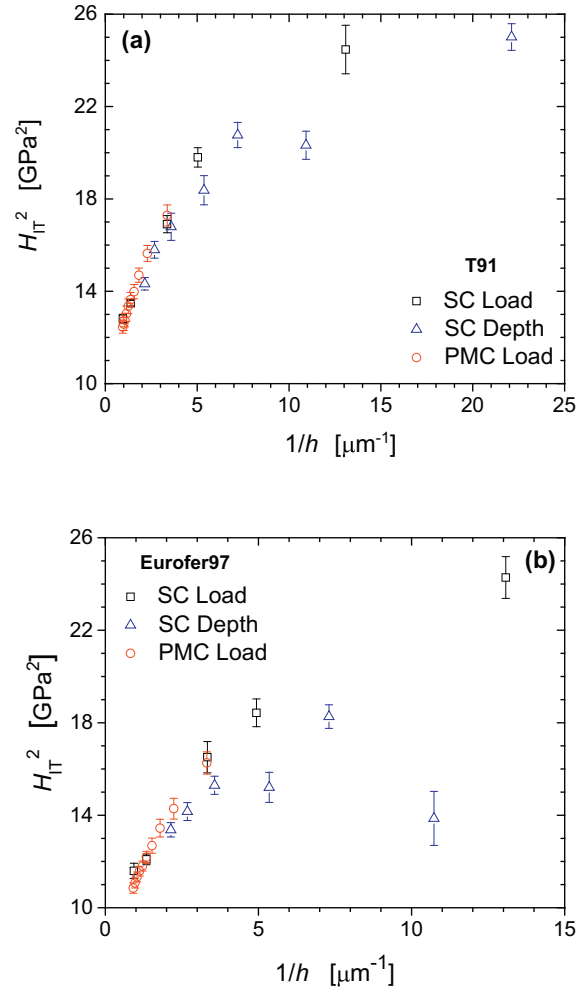


**Fig. 4.** Nix–Gao plots of the quasi-static ISE in T91 (a) and Eurofer97 (b) replotting data from Fig. 3 so as to reveal the breakdown of the scaling regime at low indentation depths.



Fig. 3 presents averaged values of the indentation hardness and indentation elastic modulus as a function of the contact depth measured by the three different quasi-static methods on T91 and Eurofer97. One notes good agreement amongst the different methods for both materials in the whole depth range covered, except for the depth controlled measurements done on Eurofer97 at depths below 150 nm, which may reflect pop-in effects due to the relaxation of stresses introduced in the samples during surface polishing.

The elastic property data revealed effects of pile-up behaviour and micro-residual stresses, which have not been corrected because of the comparative purpose of this work and the fact that the different quasi-static methods produced similar values. Indeed,  $E_{IT}$  values are about 20% (T91) and 30% (Eurofer97) higher than their reference values from macroscopic elastic property measurements, i.e. elastic moduli of 212 GPa and 213 GPa for T91 [19] and Eurofer97 [20], respectively, and a Poisson ratio of 0.3. This can be attributed to pile-up [21,22] and/or residual stresses intrinsic to the material or generated by polishing [23–26] effects which have not been corrected in these plots.

ISE are clearly observed in both materials as a decrease of hardness with depth, starting at about 5 GPa at 50 nm depth and decreasing to about 3.8 GPa at 1  $\mu\text{m}$ . By plotting the square of the hardness as a function of the inverse depth (Fig. 4), the characteristic linear dependence as predicted by Nix and Gao [11] is obtained for large indentation depths only, whereas for small depths the measured  $H_{IT}^2$  values fall well below the linear scaling regime.

### 2.3. Dynamic measurements

The dynamic measurements were recorded using a sampling frequency which was set 20 times higher than the frequency of the sinusoidal oscillations. The data analysis has been performed assuming an elastic deformation response during the oscillations and dynamically calculating the sample stiffness and the indentation contact depth by Eqs. (7) and (8), while applying gliding averages over five periods per point:

$$S = \frac{f_0}{h_0} \cos\phi + m\omega^2 - K_i \quad (7)$$

$$h_c = h - \varepsilon \frac{F}{S} \quad (8)$$

where  $f_0$  and  $h_0$  are the amplitudes of the force and displacement oscillations with angular frequency  $\omega$ , respectively,  $\phi$  is the phase angle shift between the excitation and the response, the oscillator mass  $m$  and force constant  $K_i$  are instrument parameters determined by dynamic calibration of the indenter oscillating in air, and  $\varepsilon$  is assumed to be 0.75 for a Berkovich indenter. Indentation hardness and modulus were then calculated from Eqs. (4) and (6), respectively.

Ten measurements were done for each sinus amplitude and frequency; however, three to seven of the indentations done at 10 Hz in Eurofer97 were discarded due to bad contact detection. Fig. 5 shows

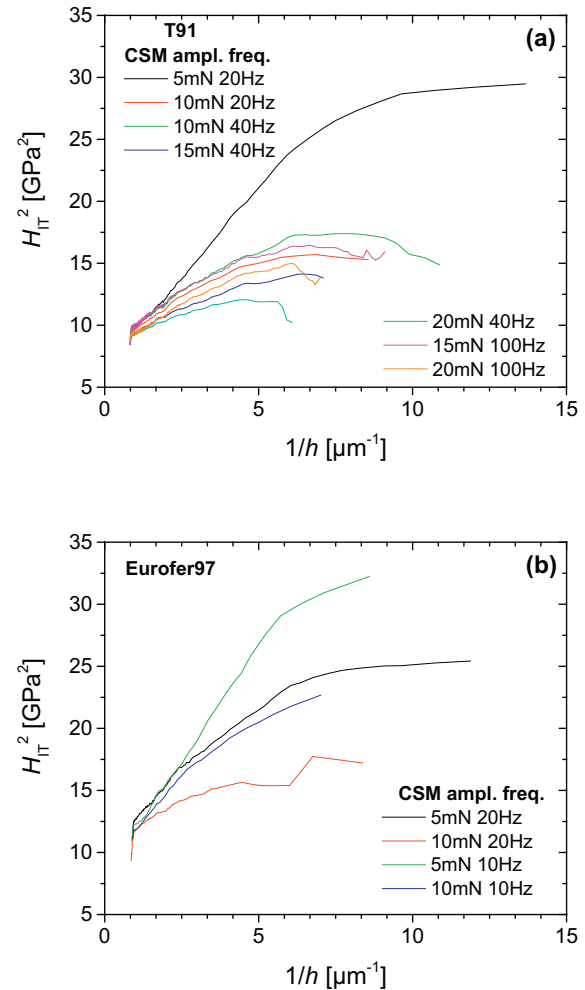
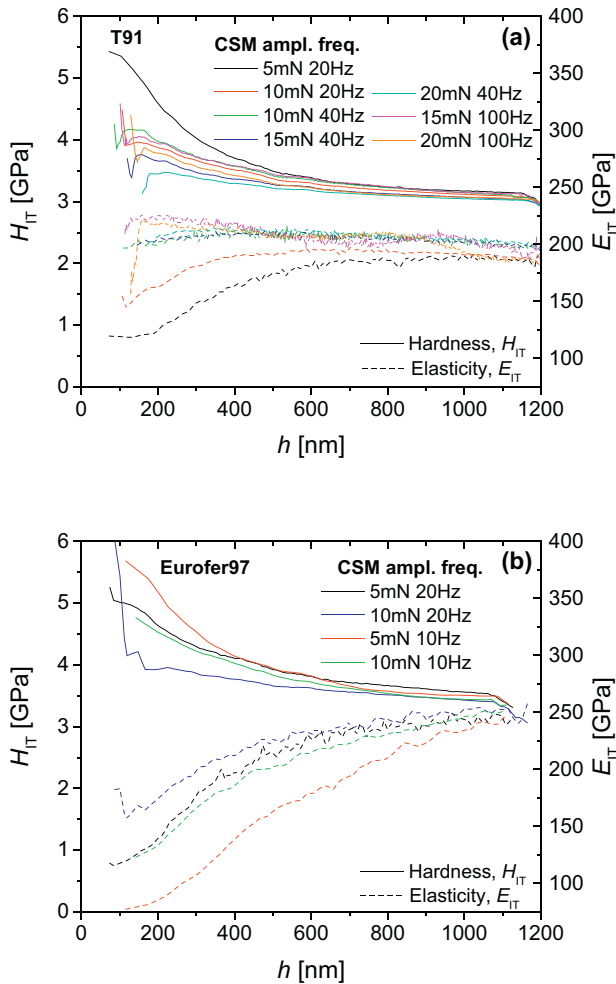


Fig. 5. Indentation hardness,  $H_{IT}$ , and indentation modulus,  $E_{IT}$ , of T91 (a) and Eurofer97 (b) measured dynamically by CSM method with different oscillation amplitudes and frequencies. Each curve represents the mean curve of 10 repeats (three to seven repeats for 10 Hz).

Fig. 6. Nix–Gao plots of the dynamic ISE in T91 (a) and Eurofer97 (b) for different oscillation amplitudes and frequencies revealing scaling breakdown.

the mean curves of indentation hardness and modulus as a function of depth calculated from the load–displacement curves, and Fig. 6 the corresponding Nix–Gao plots in terms of  $H_{IT}^2$  versus  $1/h$ . The parameters of the harmonic oscillation are indicated in the figure. Indentations with amplitude and frequency of 5 mN, 20 Hz and 10 mN, 20 Hz were recorded for both materials. Higher amplitudes and frequencies were also tested in T91, while for Eurofer97 two conditions with the same amplitudes (5 mN and 10 mN) and lower frequency (10 Hz) were applied. In all cases one notes that, for a given frequency, the indentation hardness at low depth decreases as the oscillation amplitude increases, indicating a dependence of the ISE on the oscillation parameters. Regarding the elastic properties, the indentation modulus measured using different harmonic oscillation parameters exhibits scatter at low depths, but the curves converge for large indentation depths to a value of 200 GPa for T91 and 250 GPa for Eurofer97. The variation of the measured  $E_{IT}$  at large depths is lower in the case of Eurofer97, where 11% difference between quasi-static ( $E_{IT, static} = 280$  GPa) and dynamic modulus is observed, while for T91 the variation is 20%

( $E_{IT, static} = 250$  GPa). Similarly, comparing quasi-static and dynamic methods, the variation of hardness at large depths is lower for Eurofer97 (6% difference from  $H_{IT, static} \approx 3.3$  GPa to  $H_{IT, dynamic} \approx 3.5$  GPa) than for T91 (14% difference from  $H_{IT, static} \approx 3.5$  GPa to  $H_{IT, dynamic} \approx 3.0$  GPa).

From a physical metallurgy point of view, it is important to note that the ISE, which represents a manifestation of the ‘smaller is stronger’ paradigm, is not just an inconvenient accompaniment of micro- and nano-indentation measurements that would preclude the determination of a unique hardness value for a given material. It rather represents a predictive means for the quantitative assessment of microstructural features such as the dislocation density and the characteristic length governing the size effect. Accordingly, microstructural variation due to, for instance, thermal ageing, work hardening or irradiation damage, can be quantitatively assessed through the observation of the ISE and its variation resulting from those treatments. In what follows we shall revisit the powerful framework of the ISE as developed by Nix and Gao [11], discuss certain limitations thereof, and propose a generalization which is meant to relax some of those limitations.

### 3. Modelling

#### 3.1. Indentation size effect

Nix and Gao [11] have shown that the ISE, specifically the depth dependence of the hardness values measured for crystalline materials, can be explained by using the concept of geometrically necessary dislocations (GNDs). Assuming a conical indenter with tip angle  $\theta$  relating to the indentation depth  $h$  and the contact radius  $a$ , as well as to the length of the Burgers vector  $b$  and the average spacing  $s$  of the slip steps produced by the GNDs (cf. Fig. 7), one has

$$\tan\theta = \frac{h}{a} = \frac{b}{s}, \quad \text{with } s = \frac{ba}{h}. \quad (9)$$

Nix and Gao assume the total length  $\lambda$  of the prismatic dislocation loops which are required to form the indent,

$$\lambda = \int_0^a d\lambda = \int_0^a 2\pi r \frac{dr}{s} = \frac{\pi ha}{b}, \quad (10)$$

to be homogeneously distributed over the hemispherical volume  $V = (2/3)\pi a^3$  underneath the contact area of radius  $a$ . They therefore propose the following expression for the GND density

$$\rho_{GND} = \frac{\lambda}{V} = \frac{3 \tan^2\theta}{2bh}. \quad (11)$$

The GNDs together with the statistically stored dislocations (SSDs) of density  $\rho_{SSD}$  give rise to forest strengthening which is assumed to govern the resolved shear stress according to the Taylor relation

$$\tau = \alpha \mu b \sqrt{\rho} = \alpha \mu b \sqrt{\rho_{GND} + \rho_{SSD}} \quad (12)$$

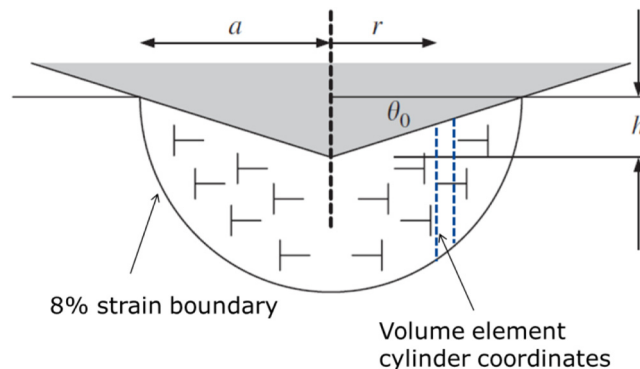


Fig. 7. Schematic of the GND loops created during indentation by a conical indenter according to Nix and Gao [11].

with  $\mu$  being the shear modulus,  $\rho$  the total dislocation density and  $\alpha \approx 0.5$  taken to be a constant. The hardness  $H$  for a given indentation depth  $h$  then derives from the shear stress according to  $H = 3\sigma = 3\sqrt{3}\tau$  with Tabor's factor of 3 and the factor  $\sqrt{3}$  stemming from the von Mises rule for the equivalent flow stress  $\sigma$ . If one combines this with Eqs. (9)–(12), one arrives at a linear relationship between the square of the hardness and the inverse of the indentation depth:

$$\left(\frac{H}{H_0}\right)^2 = 1 + \frac{h^*}{h}, \quad (13)$$

where the hardness  $H_0$  in the limit of infinite depth (macro-hardness),

$$H_0 = 3\sqrt{3}\alpha\mu b\sqrt{\rho_{SSD}}, \quad (14)$$

is governed by the SSD density, while  $h^*$  is a characteristic length that depends on the shape of the indenter, the shear modulus and  $H_0$  [11]:

$$h^* = \frac{81}{2}\alpha^2 b \tan^2\theta \left(\frac{\mu}{H_0}\right)^2. \quad (15)$$

Since the coefficients  $H_0$  and  $h^*$  both depend on the SSD density they cannot be considered strictly constant. However, as Nix and Gao pointed out  $\rho_{SSD}$  is not expected to depend on the indentation depth  $h$  but rather on the average strain in the indentation, which relates to the shape of the indenter irrespective of  $h$  (approximately 8% of strain for a Berkovich indenter with  $\theta = 19.7^\circ$ ).

The strength of the Nix–Gao model is that it has been confirmed for a wide range of indentation depths, in particular in the micro-hardness and to a lesser extent in the nano-hardness regimes, as well as for a wealth of different materials. This is quite remarkable in view of the simplicity of the model. In fact, being based on the Taylor model for strengthening by dislocation interactions, Eq. (13) depends on only two parameters,  $H_0$  and  $h^*$ . It is important to note that Eq. (13) actually predicts the ISE to be a universal phenomenon, as there is no free parameter remaining, once the dimensionless hardness  $H/H_0$  and indentation depth  $h/h^*$  have been introduced. Indeed, this universality cannot account for the diversity observed, in particular, regarding the breakdown of the scaling regime at sufficiently small depths in the nano-indentation regime, as well as differences observed with materials exhibiting either pile-up or sink-in behaviour [22,27].

Huang et al. [28] noted that there are two main reasons for possible deviations of nano-indentation hardness results from the Nix–Gao model:

1. A perfectly sharp indenter cannot be realized so that, in practice, a finite indenter tip radius will result in smaller indentation hardness values than those predicted by Eq. (13).
2. Eq. (13) is based on the idea that all GNDs are contained in a hemisphere of radius  $a$ , which implies that the GNDs are distributed uniformly in that storage volume. For  $a \rightarrow 0$  the storage volume tends to zero, while the GND density diverges.

Huang et al. [28] have addressed the second issue by introducing a maximum allowable GND density, which they use to derive a new analytic relation between indentation hardness  $H$  and depth  $h$  that agrees well with nano-indentation data of MgO and iridium [28]. They also relax the notion of uniformly distributed GNDs within the storage volume. However, as they use spherical coordinates and hence, consider the GNDs to be uniformly contained within a *spherical* shell of radius  $r$  and thickness  $dr$ , their model is not fully consistent with the notion of prismatic dislocation loops forming as the indenter is forced into the material, as these loops are considered to be contained within *cylindrical* shells.

As we shall point out in the following subsection, the proper choice of the coordinate system governs the radial dependence of the GND density which, in turn, has implications for the ISE. We will have to turn our attention to the GND density at the periphery of the indent during the indentation process, while the contact area and the concomitant plastic zone characterized by about 8% of plastic strain expand (Fig. 7). Moreover, one may argue that, in general, additional strengthening mechanisms have to be taken into account besides dislocation interactions.

### 3.2. Generalization of the Nix–Gao model

In the present subsection we outline generalizations of the Nix–Gao model and their effect on the ISE, namely the modifications stemming from (i) an additional length scale associated with an alternative strengthening mechanism, and (ii) a non-uniform distribution of GNDs described by polar coordinates and the introduction of a cut-off in the GND density.

As regards the former, one readily modifies the resolved shear stress Eq. (12) by an additive term  $k/L$ . While this modification is formally applicable for any additive strengthening mechanism, one may conveniently think of  $L$  denoting a characteristic length scale and  $k$  the strengthening coefficient associated with it. Accordingly, the hardness expression (13) is then replaced by

$$\left(\frac{H}{H_0}\right)^2 = \left(\sqrt{1 + \frac{h^*}{h}} + \frac{3\sqrt{3}k}{H_0 L}\right)^2, \quad (16)$$

which is illustrated in Fig. 8 in terms of Nix–Gao plots for various levels of the additional strength contribution. One notes that while for  $3\sqrt{3}k/LH_0$  as big as 3 the hardness quadruples, the deviation from linear scaling which is characteristic of the Nix–Gao model ( $3\sqrt{3}k/LH_0 = 0$ ) is still not very pronounced. This demonstrates the inefficacy of a constant strengthening term in explaining the observed breakdown of the scaling regime. The F/M steels of interest to the present work possess particularly high intrinsic dislocation densities which is why their strength is governed by dislocation interactions. We shall therefore neglect the  $k/L$  contribution to the strength and rather investigate the effect of the second modification.

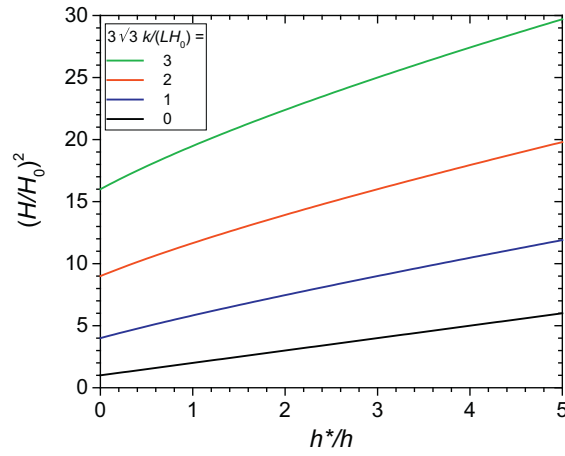


Fig. 8. Illustration of the effect of an additional strengthening term  $k/L$  of the resolved shear stress on the ISE as evidenced by Nix–Gao plots.

Instead of  $H = P/A = 3\sqrt{3} \tau$  let us consider a force  $P$  which is produced by a non-uniform pressure in an axisymmetric situation (conical indenter) as expressed by polar coordinates:

$$\rho_{\text{GND}}(r) = \frac{d\lambda}{dV} = \frac{2\pi r \frac{dr}{s}}{2\pi r l dr} = \frac{1}{s l(r)}, \quad (17)$$

where  $l(r) = \sqrt{a^2 - r^2}$  is the height of the cylindrical shell (cf. Fig. 7). The radial dependence of the GND density can then be written as [29]

$$\rho_{\text{GND}}(r; h) = \frac{\tan^2 \theta}{b h \sqrt{1 - (r/a)^2}}, \quad (18)$$

which replaces the constant GND density  $\rho_{\text{GND}} = 3 \tan^2 \theta / 2bh$  as assumed by Nix and Gao [11]. This modification is illustrated in Fig. 9, where the GND density profile of Eq. (18) is compared to a piecewise uniform distribution for  $r < a$  as implicitly assumed in Ref. [11]. Note the singular behaviour of  $\rho_{\text{GND}}(r \rightarrow a; h)$  which reflects the fact that the volume of cylindrical shell elements containing the GNDs tends to zero as one approaches the periphery of the indent. This has implications for the propagation of the plastic zone as the indentation proceeds in depth.

As a consequence one notes the integrable singularity for the modified hardness as  $r \rightarrow a$

$$H(h) = \frac{2\pi}{A} H_0 \int_0^{a=h/\tan\theta} r dr \sqrt{1 + \frac{\rho_{\text{GND}}(r; h)}{\rho_{\text{SSD}}}}, \quad (19)$$

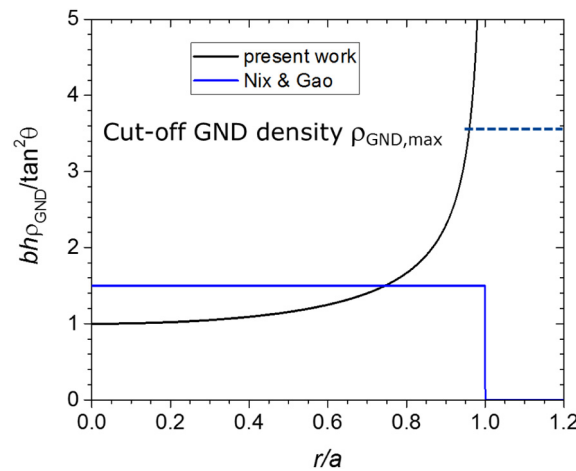


Fig. 9. Comparison of the GND density profile as compared to the piecewise uniform distribution in Ref. [11].



where  $A = \pi a^2$  is the contact area and  $H_0$  is given by Eq. (14). If one extends the integral over the whole range of GND densities,  $0 < \rho_{\text{GND}} < \infty$ , lets  $h_0 = \tan^2 \theta / b \rho_{\text{SSD}} = 2/3 h^*$  denote the characteristic length associated with the SSDs, and introduces the dimensionless inverse indentation depth  $z = h_0/h$ , one can integrate Eq. (19) to obtain

$$H(z) = \frac{1}{2} H_0 \left[ (2+z) \sqrt{1+z} - \frac{z^2}{2} \ln \frac{2\sqrt{1+z} + 2 + z}{z} \right]. \quad (20)$$

As we have not introduced a cut-off of the GND density yet, Eq. (20) does not contain any additional parameter, meaning that it is also describing universal behaviour like Eq. (13) of the Nix–Gao model, which in the present notation would read:  $H = H_0 \sqrt{1 + (3/2)z}$ . One just notes the difference in slope, while interesting enough, a quasi-linear scaling behaviour is predicted by Eq. (20) with a deviation from linearity of  $(H/H_0)^2$  vs.  $z$  amounting to <1%, which makes it practically indistinguishable from the Nix–Gao model as it cannot be detected experimentally (cf. the black and the blue curves of Fig. 10).

However, the situation changes as we introduce a cut-off of the GND density,  $\rho_{\text{GND}, \text{max}}$ , and extend the integral Eq. (19) over the domain  $0 \leq r \leq a_{\text{max}}$  only, followed by a constant continuation of the integrand for  $\rho_{\text{GND}} = \rho_{\text{GND}, \text{max}} = \text{const.}$  in the domain  $a_{\text{max}} \leq r \leq a$ . Here the transition values are given by

$$\rho_{\text{GND}, \text{max}} = \frac{\tan^2 \theta}{b h \sqrt{1 - (a_{\text{max}}/a)^2}} \quad \text{and} \quad a_{\text{max}}^2 = a^2 \left( 1 - \frac{\tan^4 \theta}{b^2 h^2 \rho_{\text{GND}, \text{max}}^2} \right). \quad (21)$$

Then one obtains

$$H(z) = \frac{1}{2} H_0 \left[ (2+z) \sqrt{1+z} - \frac{z^2}{2} \ln \frac{2\sqrt{1+z} + 2 + z}{z \left( 1 + 2\sqrt{\rho_{\text{SSD}}/\rho_{\text{GND}, \text{max}}} + (\rho_{\text{SSD}}/\rho_{\text{GND}, \text{max}})^2 + 2\rho_{\text{SSD}}/\rho_{\text{GND}, \text{max}} \right)} - z^2 \sqrt{\rho_{\text{SSD}}/\rho_{\text{GND}, \text{max}} + (\rho_{\text{SSD}}/\rho_{\text{GND}, \text{max}})^2} \right] \quad (22)$$

which reduces to the former Eq. (20) for  $\rho_{\text{SSD}}/\rho_{\text{GND}, \text{max}} \rightarrow 0$ .

Note the explicit dependence on  $\rho_{\text{SSD}}/\rho_{\text{GND}, \text{max}}$  which introduces the maximum GND density  $\rho_{\text{GND}, \text{max}}$  as an additional scaling parameter with the SSD density  $\rho_{\text{SSD}}$  acting as a reference density.

The graphs of Fig. 10 provide a comparison between the original Nix–Gao model [11] and the predictions of the present work for different values of the cut-off GND density. As already mentioned, Eq. (20) holding for  $\rho_{\text{SSD}}/\rho_{\text{GND}, \text{max}} = 0$  is practically indistinguishable from Nix–Gao model apart from its difference in slope which is, however, absorbed by the scaling parameter  $h_0$ . For finite values of  $\rho_{\text{SSD}}/\rho_{\text{GND}, \text{max}}$ , however, one notes significant deviations from the linear scaling, notably a breakdown of the scaling behaviour for small indentation depths.

The initial slope for  $z \rightarrow 0$ , as compared to the Nix–Gao model, is obtained from first-order Taylor expansion of Eq. (22), yielding  $H \approx H_0(1 + z)$  or:

$$\left( \frac{H}{H_0} \right)^2 \approx 1 + 2z \quad \text{for } z \ll 1, \quad (23)$$

which implies that the initial slope predicted by the model,  $d(H/H_0)^2/dz = 2$ , is larger than the slope predicted by the Nix and Gao model which amounts to 1.5 (Note the difference between  $h_0$  and  $h^*$ , as  $h_0 = 2/3 h^*$  (Section 3.2)). This difference reflects an intrinsic uncertainty in identifying the characteristic lengths  $h_0$  and  $h^*$ , respectively, rather than a means to distinguish between the models.

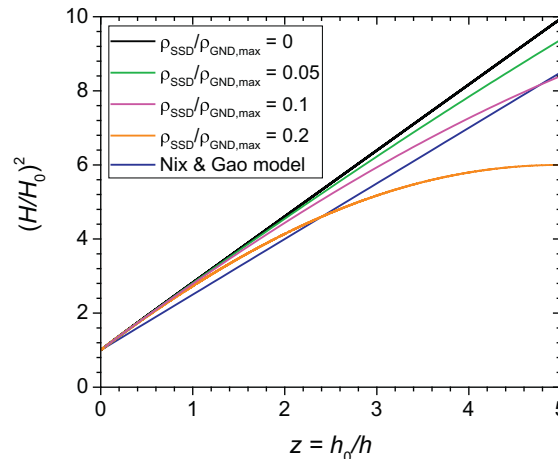


**Fig. 10.** Comparison between the original Nix–Gao model [11] and the predictions of the present work for different values of the cut-off GND density. Comparing the black (Eq. (20)) and the blue curve (Eq. (13) of the Nix–Gao model) one notes that a quasi-linear scaling behaviour is retained by the present model with a deviation from linearity amounting to <1%.

One can easily show that the depth dependent hardness, Eq. (22), exhibits a maximum at  $(\hat{z}, \hat{H})$  with

$$\hat{z} = \frac{h_0}{\hat{h}} = \frac{\rho_{\text{GND, max}}}{\rho_{\text{SSD}}}, \quad \left(\frac{\hat{H}}{H_0}\right)^2 = 1 + \frac{\rho_{\text{GND, max}}}{\rho_{\text{SSD}}} \quad (24)$$

being related through the cut-off parameter  $\rho_{\text{GND, max}}/\rho_{\text{SSD}}$ . A negative slope for  $z > \hat{z}$ , however, would imply an inverse ISE, which is considered unphysical as it is not supported by the present theoretical framework. In fact,  $z > \hat{z}$  is equivalent to  $h < \hat{h} = (\rho_{\text{SSD}}/\rho_{\text{GND, max}})h_0$  or  $h < \tan^2\theta/(b\rho_{\text{GND, max}})$  which is not admissible as the cut-off in Fig. 9 must not fall below the GND density at  $r = 0$ . This is why  $(H/H_0)^2$  attains a constant value of  $(\hat{H}/H_0)^2$  for  $z \geq \hat{z}$ .

### 3.3. Fit procedure

For an assessment of the new theoretical framework we perform a quantitative comparison with the experimental results for the F/M steels presented in Section 2. To this end, we note that the model (22) provides a robust recipe to arrive at unique sets of fit parameters as the following order is respected:

1. Fix the **reference hardness**  $H_0$  by extrapolation of hardness data to  $z = 0$  (macro-hardness), so as to make the ISE plot exhibit unit intercept:  $(H(0)/H_0)^2 = 1$ . The reference hardness  $H_0 = 3\sqrt{3}\alpha\mu b\sqrt{\rho_{\text{SSD}}}$  is governed by the SSD density.
2. Choose the **characteristic depth parameter**  $h_0$  so as to adjust the initial slope  $d(H/H_0)^2/dz = 2$  for  $z = 0$ . Note that  $h_0 = \tan^2\theta/b\rho_{\text{SSD}} = 2/3 h^*$  is the characteristic length which is also associated with the SSDs.
3. Determine the **non-dimensional cut-off of the GND density**  $\rho_{\text{GND, max}}/\rho_{\text{SSD}}$  in accordance with the incipient plateau (if corroborated by the experimental data base)  $\hat{z} = \rho_{\text{GND, max}}/\rho_{\text{SSD}}$ ,  $(\hat{H}/H_0)^2 = 1 + \rho_{\text{GND, max}}/\rho_{\text{SSD}}$ . In the absence of a plateau the parameter  $\rho_{\text{GND, max}}/\rho_{\text{SSD}}$  is chosen so as to best fit the deviation from the (quasi-)linear scaling law Eq. (20).

This procedure allows one to calculate

$$\rho_{\text{SSD}} = \frac{\tan^2\theta}{b h_0}, \quad \alpha = \frac{H_0}{3\sqrt{3}\mu b \sqrt{\rho_{\text{SSD}}}}, \quad (25)$$

$$\hat{h} = \frac{\rho_{\text{SSD}}}{\rho_{\text{GND, max}}} h_0, \quad \hat{H} = H_0 \sqrt{1 + \frac{\rho_{\text{GND, max}}}{\rho_{\text{SSD}}}}. \quad (26)$$

as material parameters derived from the three fit parameters introduced before. As a common set of constants for the F/M steels of interest, we have  $b = 0.25$  nm and  $\mu = 80$  GPa, as well as  $\theta = 19.7^\circ$  tantamount to  $\tan \theta = 0.358$  for the Berkovich indenter used in the present work. The results are presented in Table 2.

For the interpretation of the results it is interesting to recall the meaning of the fit parameters and their sensitivity to microstructural changes. Obviously, a distinction between statistically stored and geometrically necessary dislocations cannot be made at the level of individual dislocations. The shape of the indenter imprint, however, imposes a certain level of the GND density as a mean field, so that any dislocation density in excess of that level will be redundant from an indentation geometry point of view and, hence, form the SSD density. The value of  $\rho_{\text{SSD}}$  derives from the fit parameter  $h_0$  which determines the initial slope of the Nix–Gao plot.

The coefficient  $\alpha$  is characteristic of the dislocation interactions governing the flow stress, e.g. forest strengthening. We expect  $\alpha$  to be around 0.5 and any significant variation of it is indicative of a change of the prevailing strengthening mechanism. For a given value of  $\rho_{\text{SSD}}$  the value of  $\alpha$  follows from the macroscopic hardness  $H_0$  from extrapolation  $z \rightarrow 0$ .

We note that the coordinates  $(\hat{z}, \hat{H})$  of the onset of the hardness plateau (i.e. the maximum as predicted by Eq. (22)) cannot be fitted independently, because the relation  $(\hat{H}/H_0)^2 = 1 + \hat{z}$  holds according to Eq. (24). The indentation depth  $\hat{h} = (\rho_{\text{SSD}}/\rho_{\text{GND, max}})h_0$  which is characteristic of the onset of the hardness plateau and the plateau level itself,  $\hat{H}$ , are both determined by the cut-off  $\rho_{\text{GND, max}}$  and therefore do not represent independent fit parameters. In the following section we shall come back to this point which is important for an assessment of the consistency of the model and its underlying assumptions.

**Table 2**

Compilation of the fit parameters for the ISE results obtained by quasi-static single cycle (SC) and progressive multi-cycle (PMC) measurements, and the dynamic continuous stiffness measurements (CSM) on T91 and Eurofer97, cf. Eqs. (25), (26).

	T91		Eurofer97		Remark
	Quasi-static SC/PMC	Dynamic CSM	Quasi-static SC/PMC	Dynamic CSM	
$H_0$ [GPa]	3.26	2.43	3.08	2.95	
$h_0$ [nm]	105	340	125	200	
$\alpha$	0.45	0.6	0.46	0.56	0.5 [11]
$\rho_{\text{SSD}}$ [ $10^{15} \text{ m}^{-2}$ ]	4.9	1.5	4.1	2.6	4.0 [16]
$\rho_{\text{SSD}}/\rho_{\text{GND, max}}$	0.72	0.26	0.66	0.74	
$\rho_{\text{GND, max}}$ [ $10^{15} \text{ m}^{-2}$ ]	6.8	5.9	6.3	3.5	
$\hat{H}$ [GPa]	5.04	5.35	4.88	4.52	
$\hat{h}$ [nm]	76	88	83	148	

#### 4. Discussion of results

In what follows we (i) compare the measurements for the two different F/M steels with each other, (ii) confront results obtained by quasi-static and dynamic measurements, respectively, and (iii) investigate to what extent the present experimental results compare with the model developed. In doing so, the model offers a parametric framework for a quantitative comparison.

The fact that T91 and Eurofer97 are strain-rate sensitive materials with relatively large modulus-to-hardness ( $E/H$ ) ratio, in the order of 60, may contribute to the differences observed between the different nanoindentation protocols applied and to the dependence of the dynamic response on the oscillation parameters [8,30]. Leitner et al. [8] demonstrated that a changing strain rate during dwelling in quasi-static measurements was the reason of discrepancies observed between quasi-static and dynamic measurements. Significant inaccuracies in the hardness measured by CSM have been previously observed [30] and attributed to the large amount of dynamic unloading that occurs in materials with high  $E/H$  ratios, unloading that is more pronounced at larger oscillation amplitudes. In agreement with that, our dynamic results performed at the lowest amplitude (5 mN) were closest to the quasi-static values.

Application of the fit protocol presented in Section 3.3 led to satisfactory descriptions of the ISE and robust values of the fit parameters. These are presented in Figs. 11, 12 and the insets therein. It is seen that both for T91 (Fig. 11) and Eurofer97 (Fig. 12) all three quasi-static methods used here can be modelled by common fit curves for their

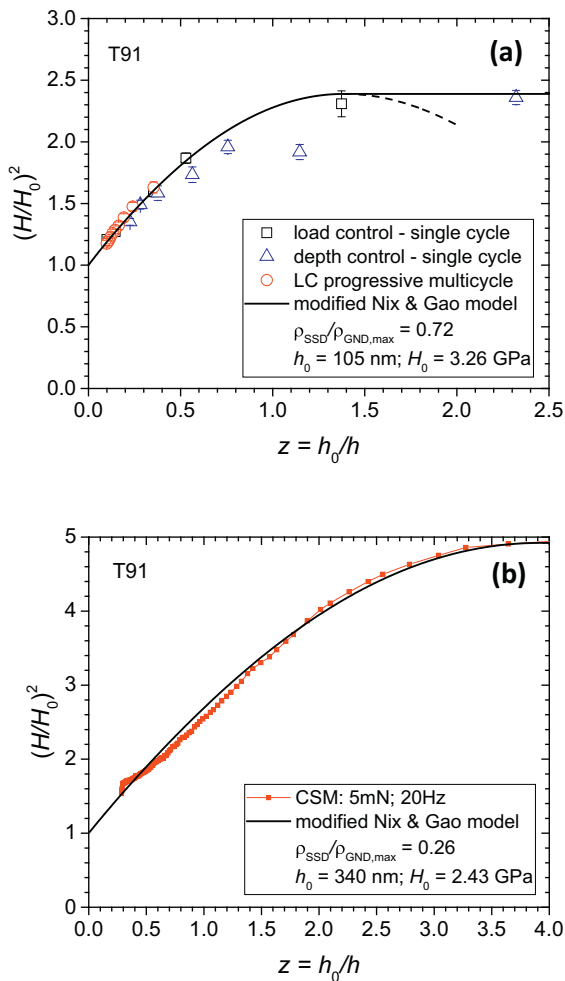


Fig. 11. Comparison between theory and experiment of the quasi-static (a) and the dynamic (b) ISE results for T91.

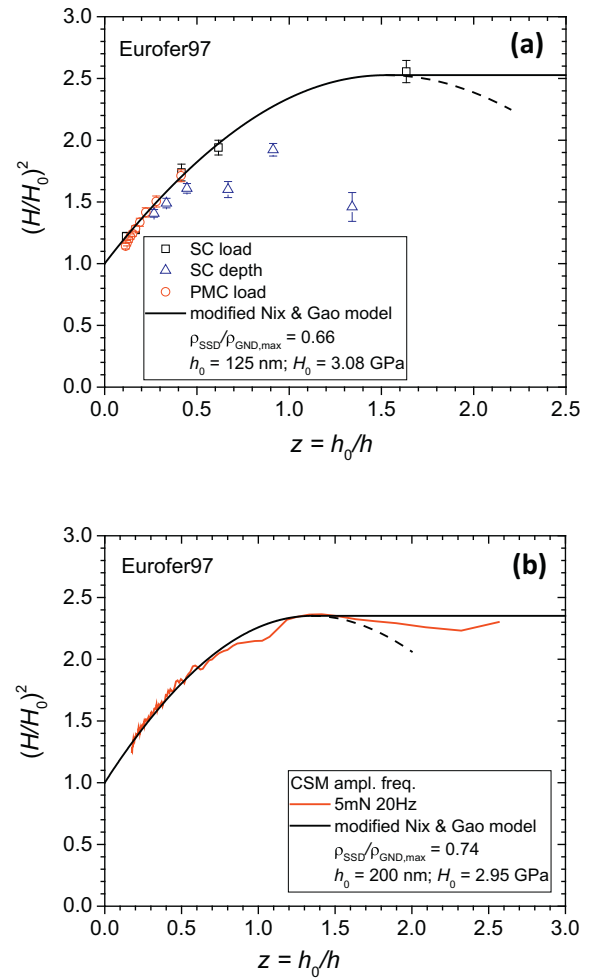


Fig. 12. Comparison between theory and experiment of the quasi-static (a) and the dynamic (b) ISE results for Eurofer97.

indentation size dependences, noting that in the case of Eurofer97 the single cycle measurements in depth control systematically underestimated the hardness for the smallest depths applied. Single cycle measurements in load control and progressive multi-cycle measurements, likewise executed in load control, yielded consistent results, while larger depth domains could be explored by the single cycle measurements.

If one compares the quasi-static measurements with the dynamic ones similar findings are made for both materials. The dynamic measurements performed at the lowest amplitude (5 mN) resulted to be closest to the quasi-static values, and will be solely reported here. Noticeable differences occurred for the T91 steel the dynamic measurements of which resulted in significantly higher values of the dimensionless saturation hardness and the corresponding dimensionless reciprocal depth, as compared to the quasi-static results.

Those values, together with all the other fit results, are compiled in Table 2. One notes that the difference in the dimensionless saturation hardness of T91 (Fig. 11(a) and (b)) is caused by the macro-hardness  $H_0$  amounting to 3.26 and 2.43 GPa for the quasi-static and the dynamic measurements, respectively. Even bigger differences are noted for the reference depth  $h_0 = 2/3 h^*$  which differs by more than a factor of three (105 and 340 nm, respectively). Although, the corresponding differences are much less pronounced in the case of the Eurofer97 steel, they are likely to result not only from measurement uncertainty, but rather reflect systematic differences of the two methods, quasi-static vs. dynamic indentation, in picking different dislocation mechanisms and deformation histories.

The  $\alpha$  parameter, however, did not exhibit significant variations for the two steels and the different indentation methods:  $\alpha$  approximately amounts to 0.5 in all cases, in agreement with the original assumption by Nix and Gao [11]. According to  $h_0 = \tan^2\theta / b\rho_{SSD}$ , noticeable variations occurred with regard to the fit values of the SSD density which were >50% and >200% higher for the quasi-static measurements of Eurofer97 and T91, respectively, as compared to their dynamic counterparts. Differences in the cut-off values for the GND densities,  $\rho_{GND,max}$ , turned out to be much less pronounced. It is important to note that all dislocation densities were extremely high, that is well above  $10^{15} \text{ m}^{-2}$ , with the maximum total dislocation density at the periphery of the plastic zone,  $\rho_{SSD} + \rho_{GND,max}$ , even exceeding  $10^{16} \text{ m}^{-2}$  as regards the quasi-static measurement results for both steels.

As regards the physical interpretation of the characteristic length  $h_0$  in terms of microstructural features we recall that  $h_0 = \tan^2\theta / b\rho_{SSD}$  relates to the SSD density. Here it is important to note that ‘statistically stored’ refers to redundancy with respect to the geometry of the indentation process, while these SSDs may well be ‘geometrically necessary’ for another reason. In fact, with  $\rho_{SSD}$  in excess of  $10^{15} \text{ m}^{-2}$  (Table 2), we are led to associating it with the high dislocation densities which are necessary to account for the misorientation of the martensite lath boundaries, for which values of  $3.0 \times 10^{15} \text{ m}^{-2}$  from electron backscatter diffraction [31] to  $4.0 \times 10^{15} \text{ m}^{-2}$  from neutron diffraction [16] have been reported. Accordingly  $\rho_{SSD}$  is the dislocation density of the martensitic lath structure which pre-exists prior to the plastic deformation by nanoindentation and the increase of which during deformation is small [16]. The characteristic length  $h_0$  is then determined by the width of the lath structure. In fact, this is in accordance with the observed dissociation of the repeat tested CSM-based hardness data, as measured at different positions for small contact depths ( $h < 200 \text{ nm}$ ), with the  $H_{IT}$  for the harder (martensitic) phase exceeding that for the softer (ferritic) phase by about 30%.

The other characteristic length  $\hat{h} = \tan^2\theta / b\rho_{GND,max}$  has the same structure but with  $\rho_{SSD}$  replaced by the cut-off GND density  $\rho_{GND,max}$ . This is the maximum of the density of GNDs which are nucleated at the periphery of the plastic zone as it is expanding. This dislocation density relates to the deformation process and is expected to contribute to a polygonization of the lath structure, so that  $\hat{h}$  may be associated with the subgrain boundary size at the plastic zone boundary. With the average of the quasi-static and dynamic measurements of the two steels given by  $h_0/\hat{h} \approx 2$ , as reported in Table 2, we expect the structure at the edge of the plastic zone to be refined as GNDs are punched downward into the material.

We recall that the level of the hardness plateau (i.e. the maximum of Eq. (22)) and the depth value of its onset cannot be fitted independently, because the relation  $(\hat{H}/H_0)^2 = 1 + \hat{z}$  holds according to Eq. (24). The fact that, to a satisfactory extent, both fit values match simultaneously for the T91 and the Eurofer97 steel can then be taken as independent evidence of the predictive power of the ISE model developed here.

## 5. Conclusions

Nano- and micromechanical testing is an important tool for the assessment of damage induced by neutron irradiation (minimized volume of activated material) and ion irradiation (limited penetration depth) the latter being of interest for the emulation of neutron irradiation damage. Besides validated experimental methods also a robust theoretical framework for the assessment of the results is required. That is what the present work is meant to contribute to.

Indentation size effects of the F/M steels T91 and Eurofer97 have been investigated by quasi-static and dynamic nanoindentation methods. The quasi-static methods (depth-controlled and force-controlled single cycles, and force-controlled progressive multi-cycle

measurements) show good agreement, while continuous stiffness measurements turn out to be amplitude dependent. A modification to the Nix–Gao framework of the indentation size effect has been introduced in order to describe the breakdown of the scaling regime. The modification consists in properly accounting for the GND density profile. The generalized model of the ISE captures the extremely high dislocation density associated with martensitic lath boundary misorientation.

Different results obtained when the model is fitted for depth or force controlled quasi-static vs. dynamic indentation methods are supposed not to be spurious, i.e. caused by measurement uncertainty, but distinct fit values may rather reflect differences in the deformation mechanisms and histories notably the expansion of the plastic zone associated with the different indentation methods.

## Acknowledgements

The authors would like to express their gratitude to Dr. O. Dieste-Blanco (JRC) for his kind assistance with the TEM imaging.

This work has been supported by the EURATOM Direct Actions. It contributes to the European Energy Research Alliance – Joint Programme on Nuclear Materials (EERA JPNM), in particular to the EERA JPNM pilot project NINA – NanoIndentation for Nuclear Applications.

The experimental part of the work has been performed in the framework of nine laboratories engaged in a more comprehensive round robin exercise within EERA JPNM, the results of which will be presented elsewhere.

## Data availability

The force-controlled single cycles raw data required to reproduce these findings are available to download from <https://odin.jrc.ec.europa.eu>. The raw data of the other measurements methods cannot be shared at this time due to technical limitations.

## References

- [1] P. Hosemann, C. Shin, D. Kiener, Small scale mechanical testing of irradiated materials, *J. Mater. Res.* 30 (2015) 1–15.
- [2] C.D. Hardie, S.G. Roberts, A.J. Bushby, Understanding the effects of ion irradiation using nanoindentation techniques, *J. Nucl. Mater.* 462 (2015) 391–401.
- [3] C. Heintze, F. Bergner, S. Akhmedaliev, E. Altstadt, Ion irradiation combined with nanoindentation as a screening test procedure for irradiation hardening, *J. Nucl. Mater.* 472 (2016) 196–205.
- [4] C.A. Schuh, Nanoindentation studies of materials, *Mater. Today* 9 (2006) 32–40.
- [5] D.F. Bahr, D.J. Morris, Nanoindentation: localized probes of mechanical behavior of materials, in: Sharpe (Ed.), *Springer Handbook of Experimental Solid Mechanics*, Springer 2008, pp. 389–407.
- [6] K.W. Siu, A.H.W. Ngan, Oscillation-induced softening in copper and molybdenum form nano- to micro-length scales, *Mater. Sci. Eng. A* 572 (2013) 56–64.
- [7] M.J. Cordill, N.R. Moody, W.W. Gerberich, Effects of dynamic indentation on the mechanical response of materials, *J. Mater. Res.* 23 (2008) 1604–1613.
- [8] A. Leitner, V. Maier-Kiener, D. Kiener, Dynamic nanoindentation testing: is there an influence on a material's hardness? *Math. Res. Lett.* (2017) <https://doi.org/10.1080/21663831.2017.1331384>.
- [9] K. Durst, M. Göken, G.M. Pharr, Indentation size effect in spherical and pyramidal indentations, *J. Phys. D. Appl. Phys.* 41 (2008), 074005.
- [10] J.G. Swadener, E.P. George, G.M. Pharr, The correlation of the indentation size effect measured with indenters of various shapes, *J. Mech. Phys. Solids* 50 (2002) 681–694.
- [11] W.D. Nix, H. Gao, Indentation size effects in crystalline materials: a law for strain gradient plasticity, *J. Mech. Phys. Solids* 46 (1998) 411–425.
- [12] K. Durst, B. Backes, O. Franke, M. Göken, Indentation size effect in metallic materials: modeling strength from pop-in to macroscopic hardness using geometrically necessary dislocations, *Acta Mater.* 54 (2006) 2547–2555.
- [13] Z. Yuan, F. Li, B. Chen, F. Xue, The correlation between indentation hardness and material properties with considering size effects, *J. Mater. Res.* 29 (2014) 1317–1325.
- [14] J.G. Swadener, A. Misra, R.G. Hoagland, M. Nastasi, A mechanistic description of combined hardening and size effects, *Scr. Mater.* 47 (2002) 343–348.
- [15] X. Hou, N. Jennett, Application of a modified slip-distance theory to the indentation of single-crystal and polycrystalline copper to model the interactions between indentation size and structure size effects, *Acta Mater.* 60 (2012) 4128–4135.
- [16] S. Harjo, T. Kawasaki, W. Gong, K. Aizawa, Dislocation characteristics in lath martensitic steel by neutron diffraction, *J. Phys. Conf. Ser.* 746 (2016), 012046.

- [17] K. Herrman, N.M. Jennett, W. Wegener, J. Meneve, K. Hasche, R. Seemann, Progress in determination of the area function of indenters used for nanoindentation, *Thin Solid Films* 377–378 (2000) 394–400.
- [18] J. Woigard, J.C. Dargenton, C. Tromas, V. Audurier, A new technology for nanohardness measurements: principle and applications, *Surf. Coat. Technol.* 100–101 (1998) 103–109.
- [19] C. Cristalli, J. Rantala, C. Heintze, M. Pouchon, Mechanical Properties From Indentation Tests, Nanoindentation and Micro-mechanical Testing. Deliverable D2.4 and D2.5, 2014 (MATTER project, Grant Agreement no. 269706).
- [20] T. Martin, S. Knaak, Y. Zhong, J. Aktaa, Ultrasonic testing on Eurofer welded joints for determination of the minimum detectable flaw size, *KIT Scientific Reports* 7543, TW6-TTMS-005, D5, 2010.
- [21] N. Moharrami, S.J. Bull, A comparison of nanoindentation pile-up in bulk materials and thin films, *Thin Solid Films* 572 (2014) 189–199.
- [22] J.D. Gale, A. Achuthan, The effect of work-hardening and pile-up on nanoindentation measurements, *J. Mater. Sci.* 49 (2014) 5066–5075.
- [23] G.M. Pharr, E.G. Herbert, Y. Gao, The Indentation Size Effect: a critical examination of experimental observations and mechanistic interpretations, *Annu. Rev. Mater. Res.* 40 (2010) 271–292.
- [24] Y. Ding, R.R. Chromik, Relationship between indentation plastic zone size and residual stresses in plastically deformed Fe, *Mat. Sci. Eng. A* 696 (2017) 1–9.
- [25] J. Jang, Estimation of residual stress by instrumented indentation: a review, *J. Ceram. Process. Res.* 10 (3) (2009) 391–400.
- [26] K.S. Chen, T.C. Chen, K.S. Ou, Development of semi-empirical formulation for extracting materials properties from nanoindentation measurements: residual stresses, substrate effect, and creep, *Thin Solid Films* 516 (2008) 1931–1940.
- [27] G. Muthupandya, K.R. Limb, Y.S. Nab, et al., Pile-up and sink-in nanoindentation behaviors in AlCoCrFeNi multi-phase high entropy alloy, *Mater. Sci. & Eng. A* 696 (2017) 146–154.
- [28] Y. Huang, et al., A model of size effects in nano-indentation, *J. Mech. Phys. Solids* 54 (2006) 1668–1686.
- [29] M. Zhao, W.S. Slaughter, M. Li, S.X. Mao, Material-length-scale-controlled nanoindentation size effects due to strain-gradient plasticity, *Acta Mater.* 51 (2003) 4461–4469.
- [30] G.M. Pharr, J.H. Strader, W.C. Oliver, Critical issues in making small-depth mechanical property measurements by nanoindentation with continuous stiffness measurement, *J. Mater. Res.* 24 (2009) 653–666.
- [31] T. Berecz, P. Jenei, A. Csore, et al., Determination of dislocation density by electron backscatter diffraction and X-ray line profile analysis in ferrous lath martensite, *Mater. Charact.* 113 (2016) 117–124.